Article

Dissolution-Driven Convection in a Porous Medium Due to Vertical Axis of Rotation and Magnetic Field

Gundlapally Shiva Kumar Reddy [1] , **Nilam Venkata Koteswararao** [2], **Ragoju Ravi** [1] , **Kiran Kumar Paidipati** [3] and **Christophe Chesneau** [4],*

1. Department of Applied Sciences, National Institute of Technology Goa, Ponda 403401, India; gshivakumarreddy913@nitgoa.ac.in (G.S.K.R.); ravi@nitgoa.ac.in (R.R.)
2. The School of Advanced Sciences and Languages, VIT Bhopal University, Sehore 466114, India; nilam.venkatakoteswararao@vitbhopal.ac.in
3. Area of Decision Sciences, Indian Institute of Management Sirmaur, Sirmaur 173025, India; kkpaidipati@iimsirmaur.ac.in
4. Laboratoire de Mathématiques Nicolas Oresme (LMNO), Université de Caen Normandie, Campus II, Science 3, 14032 Caen, France
* Correspondence: christophe.chesneau@unicaen.fr

Abstract: This article aims to study the effect of the vertical rotation and magnetic field on the dissolution-driven convection in a saturated porous layer with a first-order chemical reaction. The system's physical parameters depend on the Vadasz number, the Hartmann number, the Taylor number, and the Damkohler number. We analyze them in an in-depth manner. On the other hand, based on an artificial neural network (ANN) technique, the Levenberg–Marquardt backpropagation algorithm is adopted to predict the distribution of the critical Rayleigh number and for the linear stability analysis. The simulated critical Rayleigh numbers obtained by the numerical study and the predicted critical Rayleigh numbers by the ANN are compared and are in good agreement. The system becomes more stable by increasing the Damkohler and Taylor numbers.

Keywords: linear stability; magnetic field; porous layer; chemical reaction; Levenberg–Marquardt backpropagation algorithm

1. Introduction

Dissolution-driven convection occurs in the host phase of a partially miscible system when a buoyantly unstable density stratification develops upon dissolution. The onset of convection in a porous layer has received considerable interest in science, engineering, and technology, such as food engineering, oil recovery, chemical reactor design, and plastic processing. Dissolution-driven convection in porous media has received recent interest in the context of the long-term geological storage of carbon dioxide in the underground, natural, brine-filled caverns, often referred to as saline aquifers, in the production of mineral deposits, and a variety of other applications. Following injection into the saline aquifer, dissolution of supercritical carbon dioxide in the host brine causes a local density increase, leading to gravitational instability of the diffusive boundary layer and the formation of convective fingers [1–6]. In addition, Benard and chemical instabilities were studied for the dissociation of a horizontal layer of Navier–Stokes fluid due to the Boussinesq approximation. Dissolution-driven convection of a binary fluid in a reactive porous layer was foremost studied [7,8], then secondary instabilities [9], and constant temperatures and chemical equilibrium in binary fluid at the boundary surfaces while the solubility of the dissolved issue relies upon temperature [10–18]. The diffusive boundary layer becomes unstable in anisotropic porous media where both the capillary transition zone and dispersion are considered, even if the geochemical reaction is significantly large. While the reaction enhances stability by consuming the solute, porous media anisotropy, hydrodynamic dispersion, and capillary transition zone destabilize the diffusive boundary layer

that is unstably formed in a gravitational field [19–21]. Stability techniques that look at and broaden the way the solute's dissolution influences the thermal convection and prolongs this evaluation by the use of an asymptotic energy method, Galerkin and spectral techniques, are expecting the structure of the preliminary bifurcation. Darcy, Darcy Brinkmann, and Darcy Lapwood Brinkmann's models were used to study porous, anisotropic porous, and sparsely packed porous medium over multiple diffusive convection [22–25].

Exhausting the magnetic field is an adequate method to regulate a thermally induced flow. The magnetic field will propagate a Lorentz force to permeate the convective flow. The penetration effect depends on the strength of the applied magnetic field and its assimilation into the convective flow direction. The magnetic field is significant for engineering applications such as magnetohydrodynamics, cooling of nuclear reactors, micropump electronic packages, and microelectronic devices. The density can be enhanced or reduced depending on the magnetic field and electrode configuration. The magnetic field effect on formally charged transfer-controlled active dissolution and the Lorentz force reduces the field gradient force, which boosts active dissolution. The convective cavities of various aspect ratios in the magnetohydrodynamics of fluids are broadly studied [26–38]. Due to the simultaneous action of buoyancy and induced magnetic forces, heat transfer to liquid metals may be significantly affected by the presence of a magnetic field, but very small effects are experienced by other fluids. The Coriolis and centrifugal buoyancy forces arising from rotation have a remarkable influence on the local heat transfer when compared with the nonrotating results. A series of interferograms, stream functions, and isotherm plots demonstrated the strong effect of rotation on the flow field and heat transfer. A correlation of the Nusselt number as a function of Taylor and Rayleigh numbers is presented [15,19,39–42].

Various machine learning techniques, in particular artificial neural networks (ANN), have been widely used in different research areas for predicting data. Recently, many researchers have used ANN to predict the data and compare them with their results. Neural networks are used to solve different types of large data-related problems and solve the Navier–Stokes equations for turbulence by using the Bayesian cluster. The combination of ANN and gene expression programming compares the local Nusselt number with their numerical results [43–45]. The investigation of bifurcating fluid phenomena using a reduced-order modeling setting was aided by artificial neural networks, ANNs, to study the flow and thermal fields of the onset of convection in a rectangular channel. From their results, they found that the ANN can precisely predict the Nusselt number with less computational time and cost compared to the DNS [46–51].

The purpose of this article is to explore the magnetic effect, the Coriolis effect, and chemical reaction effects on the onset of convection in a porous medium. To the best of our knowledge, linear stability theory and ANN prediction of threshold Rayleigh number for the onset of magneto-rotating convection in a porous medium with first-order chemical reaction have not been studied so far. The plan for this article is as follows: Section 2 describes the mathematical modeling under consideration, Section 3 presents the ANN methodology, and Section 4 discusses the results. The paper ends with a conclusion in Section 5.

2. Mathematical Modeling

2.1. Basic Equations

Consider an electrically conducting fluid-saturated porous layer of thickness d that is salted from below and confined between two parallel horizontal planes at $z = 0$ and $z = d$. The horizontal coordinate x and vertical coordinate z increase upwards in a Cartesian coordinate with the origin at the bottom of the porous medium. The surfaces are extended infinitely in x and y directions and a constant salinity gradient C is maintained across the porous layer. Let $\Omega = \Omega \hat{e}_z$ be the constant angular velocity of the layer. To make the Boussinesq approximation valid, the physical properties of the fluid are assumed to be constant, except for density in the buoyancy term. The porous medium is considered

homogeneous and isotropic. Based on [15,19,39,40], with the physical configuration recalled in Figure 1, the governing equations are

$$\nabla \cdot \mathbf{u} = 0, \tag{1}$$

$$\rho_0 Ca \frac{\partial u}{\partial t} + \frac{\mu}{K}\mathbf{u} = -\nabla p + \rho_0 g \beta_c (C - C_0)\hat{e}_z + \sigma_1(\mathbf{u} \times B_0\hat{e}_z) \times B_0\hat{e}_z - \frac{2\rho_0\Omega}{\delta}\hat{e}_z \times \mathbf{u}, \tag{2}$$

$$\epsilon \frac{\partial C}{\partial t} + (\mathbf{u} \cdot \nabla)C = \epsilon D_v \nabla^2 C - \beta C, \tag{3}$$

subject to the following boundary conditions

$$\mathbf{u} = 0, \ C = C + \Delta C \text{ on } z = 0,$$
$$\mathbf{u} = 0, \ C = C_0, \text{ on } z = d. \tag{4}$$

Here, Ca, μ, K, p, ρ, β_c, g, t, ϵ, D_v, and β are the acceleration coefficient, dynamic viscosity, permeability, dynamic pressure, reference density, solute expansion coefficient, gravity acceleration, time, porosity, solute diffusion coefficient, and reaction rate of the solute, respectively. The dimensionless quantities are given as follows:

$$x = x^*d, \qquad\qquad y = y^*d, \qquad\qquad z = z^*d,$$
$$u = \frac{\phi D_v}{d}u^*, \qquad\qquad v = \frac{\phi D_v}{d}v^*, \qquad\qquad w = \frac{\phi D_v}{d}w^*,$$
$$t = \frac{d^2}{D_v}t^*, \qquad\qquad C = C_0 C^*, \tag{5}$$

as well as the non-dimensional quantities

$$Ra = \frac{g\rho_0\beta_c\Delta CKd^n}{\phi^n\mu D_v^n}, \qquad\qquad Dm = \frac{\beta d^2}{\phi D_v}, \qquad\qquad Ha = \frac{\sigma_1 B_0^2 K}{\mu},$$
$$Ta = \frac{2\rho_0\Omega\kappa_f}{\mu\phi}, \qquad\qquad Va = \frac{\mu d^2}{\rho_F C_a K D_v}, \tag{6}$$

where Ra, Ta, Ha, Dm, and Va are the Rayleigh number, Taylor number, Hartmann number, Damkohler number, and Vadasz number, respectively. The non-dimensional form of the governing Equations (1)–(3) and the corresponding boundary conditions (4) are given by

$$\nabla.\mathbf{u} = 0, \tag{7}$$

$$\frac{1}{Va}\frac{\partial \mathbf{u}}{\partial t} + \mathbf{u} = -\nabla p + RaC\hat{e}_z + Ha^2[(\mathbf{u} \times \hat{e}_z) \times \hat{e}_z] - Ta\hat{e}_z \times \mathbf{u}, \tag{8}$$

$$\frac{\partial C}{\partial t} + (\mathbf{u}.\nabla)C = \nabla^2 C - DmC, \tag{9}$$

subject to the boundary conditions

$$\mathbf{u} = 0, \ C = 1 \text{ on } z = 0,$$
$$\mathbf{u} = 0, \ C = 0 \text{ on } z = 1. \tag{10}$$
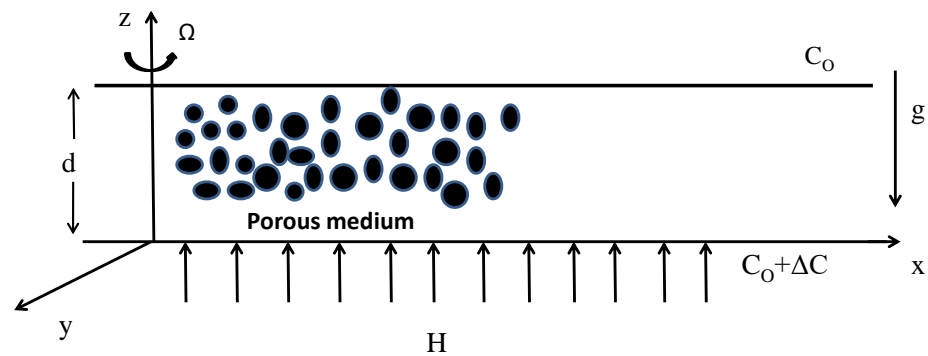
Figure 1. Physical configuration.

2.2. Basic Flow

The basic stationary flow of Equations (7)–(10) is as follows:

$$u_b = 0, \tag{11}$$

$$C_b = 1 - z. \tag{12}$$

2.3. Linear Stability Analysis

The perturbation of the basic state for the Equations (7)–(10) is

$$\mathbf{u} = u_b + U', \ C = C_b + C', \ p = P_b + P'. \tag{13}$$

By substituting Equation (13) into Equations (7)–(10), one obtains

$$\nabla U' = 0 \tag{14}$$

$$\frac{1}{Va}\frac{\partial U'}{\partial t} + U' = -\nabla P' + RaC'\hat{e}_z + Ha^2[(U' \times \hat{e}_z) \times \hat{e}_z] - Ta\hat{e}_z \times U', \tag{15}$$

$$\frac{\partial C'}{\partial t} = w' + \nabla^2 C' - DmC', \tag{16}$$

subject to the boundary conditions

$$U' = 0, \ C' = 0 \text{ on } z = 0,$$
$$U' = 0, \ C' = 0 \text{ on } z = 1. \tag{17}$$

By taking the third component of the curl of Equation (15) and curl of curl of Equation (15), one obtains

$$\left(1 + \frac{1}{Va}\frac{\partial}{\partial t} - Ha^2\right)w_z - Ta^{1/2}\frac{\partial w'}{\partial z} = 0, \tag{18}$$

$$\left(\frac{1}{Va}\nabla^2\frac{\partial}{\partial t} + \nabla^2 + Ha^2\frac{\partial^2}{\partial z^2}\right) - Ra\nabla_h^2 C' + Ta^{1/2}\frac{\partial w_z}{\partial z} = 0. \tag{19}$$

From Equations (16), (18) and (19), we obtain

$$\left[D_2\left(D_1 D_3 + Ta\frac{\partial^2}{\partial z^2}\right) - Ra\nabla_h^2 D_1\right]w' = 0, \tag{20}$$

where

$$D_1 = 1 + \frac{1}{Va}\frac{\partial}{\partial t} - Ha^2, \tag{21}$$

$$D_2 = \frac{\partial}{\partial t} - \nabla^2 + Dm, \tag{22}$$

$$D_3 = \frac{1}{Va}\nabla^2\frac{\partial}{\partial t} + \nabla^2 + Ha^2\frac{\partial^2}{\partial z^2}. \tag{23}$$

Let us introduce the normal mode by writing that the perturbation is in the form of

$$w' = e^{i(lx+my)+\sigma t}\sin(\pi z), \tag{24}$$

where l and m are the wave numbers along x and y directions and σ is a complex parameter. Substituting Equation (24) into Equation (20), one obtains

$$Ra = \frac{\sigma + \delta^2 + Dm}{q^2}\left(\frac{1}{Va}\sigma\delta^2 + \delta^2 + Ha^2\pi^2\right) + \frac{Ta\pi^2(\sigma + \delta^2 + Dm)}{q^2\left(1 + \frac{\sigma}{Va} - Ha^2\right)}, \tag{25}$$

where $q^2 = l^2 + m^2$ and $\delta^2 = \pi^2 + q^2$.

2.4. Stationary Mode

To study the stationary stability, take $\sigma = 0$ in the Rayleigh number for the exchange of the stabilities at the onset of stationary convection, say Ra_{sc}. It is given as

$$Ra_{sc} = \frac{\delta^2 + Dm}{q^2}\left(\delta^2 + Ha^2\pi^2\right) + \frac{Ta\pi^2(\delta^2 + Dm)}{q^2(1 - Ha^2)}. \tag{26}$$

The critical Rayleigh number at the onset of stationary convection Ra_c^{sc} is

$$Ra_c^{sc} = Dm + 2\pi\sqrt{\frac{(Dm + \pi^2)(-1 + Ha^4 - Ta)}{Ha^2 - 1}} + \frac{\pi(-2 + Ha^2 + Ha^4 - Ta)}{Ha^2 - 1}. \tag{27}$$

The above stationary Rayleigh number reduces to $Ra_{sc} = \frac{\delta^4}{q^2}$ with the critical values $Ra_c^{sc} = 4\pi^2$, $q_c^{sc} = \pi$ in the absence of a magnetic field, Coriolis effect, and chemical reaction effect, which agrees with the results of Horton and Rogers [41] and Lapwood [42] for the onset of convection in a porous layer.

2.5. Oscillatory Mode

To study the oscillatory stability, take $\sigma = i\omega$. The Rayleigh number at the onset of oscillatory convection is

$$Ra_{oc} = \frac{\delta^4\omega^4 + \alpha_1\omega^2 + \alpha_2}{q^2Va[(-1 + Ha^2)^2Va^2 + \omega^2]}, \tag{28}$$

where

$$\alpha_1 = Va\pi^2(DmHa^2 + TaVa) + (Dm + Ha^2\pi^2)\delta^2 - (-1 + Ha^2)^2Va\delta^4, \tag{29}$$

$$\alpha_2 = -Da^4 + (-1 + Ha^2)(Dm + Ha^2\pi^2) - \pi^2Ta)\delta^2 + \\ (-1 + Ha^2)Va^3\left[Dm\pi^2(-Ha^2 + Ha^4 - Ta)\right]\delta^4 + -\delta^6, \tag{30}$$

$$\omega^2 = -(-1 + Ha^2)^2Va^2 + \frac{\pi^2Ta\left[Dm + (-1 + Ha^2)Va + \delta^2\right]}{Ha^2\pi^2Va + \delta^2(Dm + Va + \delta^2)}. \tag{31}$$

3. Artificial Neural Network Modeling

Let us now present some basis for the ANN modeling. An ANN is a computing system based on biological neural networks (which are interconnected) that resemble a brain. In general, ANN can be used to predict data. In this study, we used a network with three layers: input, hidden, and output, as well as other components, such as feed-forward propagation, an optimal number of neurons, and backpropagation (update weights and biases) (see Figures 2 and 3). To train the suggested network, we use the Levenberg–Marquardt backpropagation algorithm, as proposed by Yu and Wilamowski [46]. To prepare the organization, data are first divided into three groups. A total of 650 datasets were utilized to train, test, and validate the ANN model, with 70%, 15%, and 15% of the data being randomly allocated for preparing and assessing. The optimal number of neurons (Nn) for the best performing artificial neural network architecture is determined by examining three different statistical values: coefficient of determination (R^2), root mean square error ($RMSE$), and root mean relative error ($RMRE$), which are defined by

$$R^2 = 1 - \frac{\sum_i^N (Ra_{c,s} - Ra_{c,a})^2}{\sum_i^N (Ra_{c,s} - \overline{Ra_{c,a}})^2},$$

$$RMSE = \sqrt{\frac{\sum_i^N (Ra_{c,s} - Ra_{c,a})^2}{N}}$$

$$RMRE = \sqrt{\frac{1}{N} \sum_i^N \left| \frac{(Ra_{c,s} - Ra_{c,a})}{Ra_{c,s}} \right|}. \tag{32}$$

Here, $Ra_{c,s}$ is the simulated critical Rayleigh number, $Ra_{c,a}$ is the ANN critical Rayleigh number, the index i refers to the i-th experiment, bar denotes average value, and N is data size or number. See Seo et al. [45] for further details on these measures. The regression plots of training, testing, and validation for these three different sets are illustrated in Figure 4. The values of R^2, $RMSE$, and $RMRE$ for different values of Va, Ha, Ta, and Dm are illustrated in Tables 1 and 2. From these tables, it is clear that the present ANN model can predict the critical Ra for linear stability analysis for different Va, Ha, Ta, and Dm.
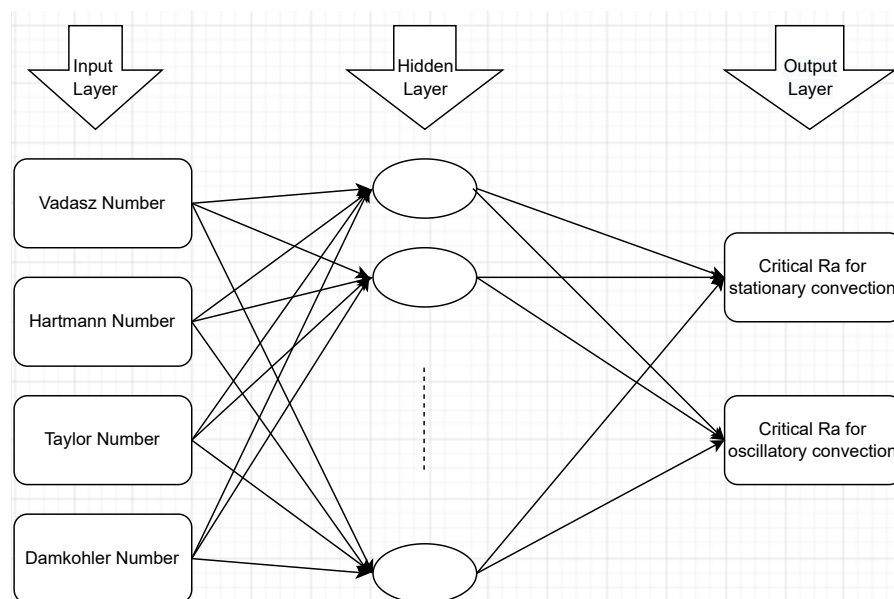
Figure 2. Schematic representation of a multilayer feed-forward network consisting of two inputs, one hidden layer, and two outputs.
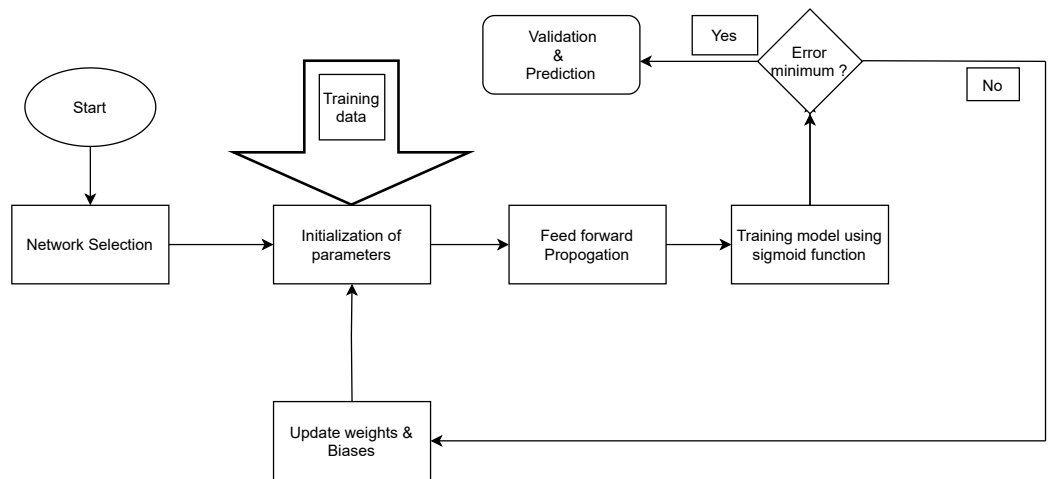
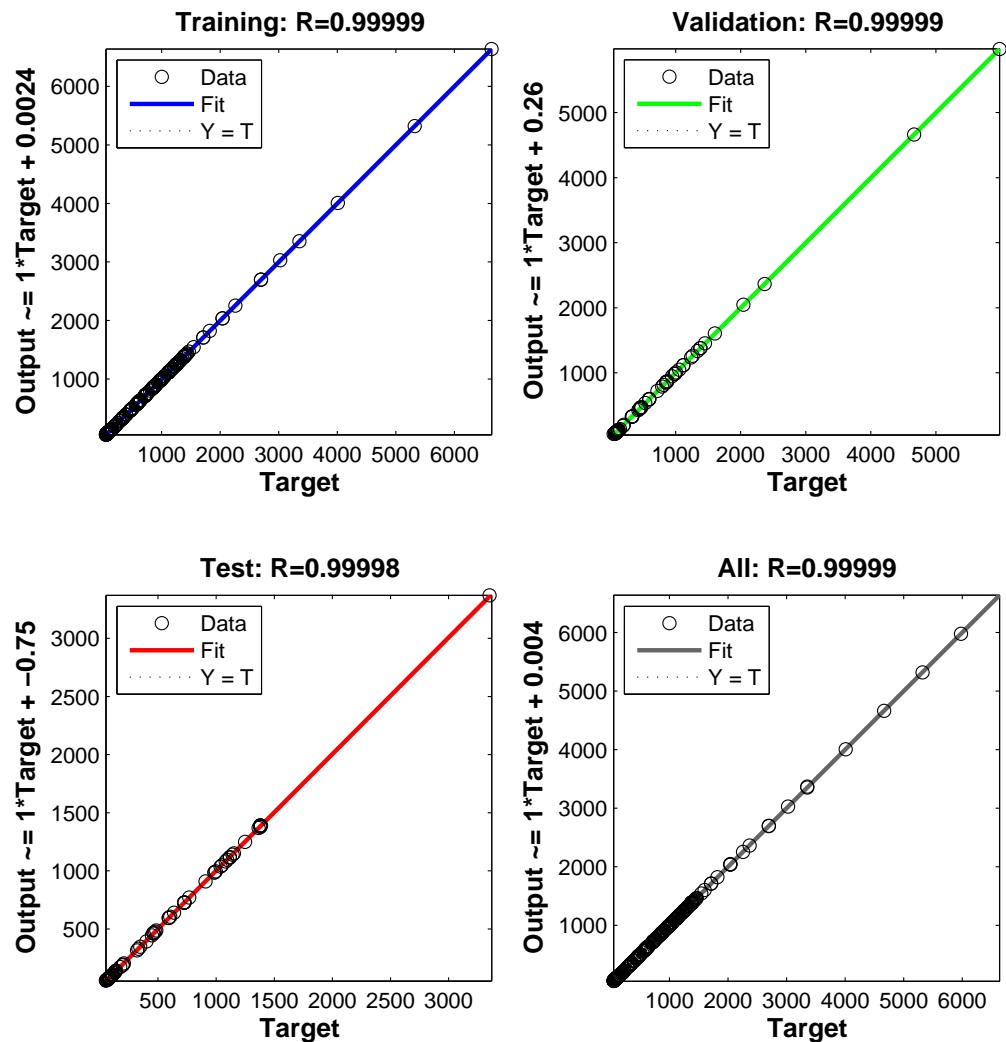**Figure 3.** Flow chart of the artificial neural network.

Figure 4. Regression plots for training, validation, and testing; the targets are simulated data and the outputs are ANN-predicted data.

Table 1. Calculated stationary values of R^2, *RMSE*, and *RMRE* at various values of *Ta*, *Dm*, and *Ha*.

Values		Stationary		
		R^2	*RMSE*	*RMRE*
$Ta = 0, 5, 10, \ldots, 50$	$Va = 0.5, Ha = 0.5, Dm = 2$	0.999992	0.301510	0.549099
$Dm = 0.5, 1, 1.5, \ldots, 5$	$Va = 0.5, Ha = 0.5, Ta = 20$	0.999991	0.316226	0.562340
$Ha = 0.1, 0.2, 0.3, \ldots, 0.9$	$Va = 0.5, Dm = 2, Ta = 20$	0.999996	0.333332	0.5773497

Table 2. Calculated oscillatory values of R^2, *RMSE*, and *RMRE* at various values of *Ta*, *Dm*, and *Ha*.

Values		Oscillatory		
		R^2	*RMSE*	*RMRE*
$Ta = 0, 5, 10, \ldots, 50$	$Va = 0.5, Ha = 0.5, Dm = 2$	0.999999	0.447213	0.668740
$Dm = 0.5, 1, 1.5, \ldots, 5$	$Va = 0.5, Ha = 0.5, Ta = 20$	0.999994	0.316226	0.562340
$Ha = 0.1, 0.2, 0.3, \ldots, 0.9$	$Va = 0.5, Dm = 2, Ta = 20$	0.999966	0.333327	0.577345

4. Discussion

The numerical results and discussion are presented in this section. In this results part, we evaluated a numerical study of the effect of the magnetic field and rotation on the onset of dissolution-driven convection saturated porous layer with ANN prediction. The critical Rayleigh number at the onset of stationary (Ra_c^{sc}) and oscillatory (Ra_c^{oc}) convection is obtained for the prescribed values of the other parameters. The investigations are performed for various values of the Hartmann number, Taylor number, Vadasz number, and Damkohler number. In Figures 5–10, solid and dotted lines represent the stationary and oscillatory convection, respectively. The following physically realistic range of these parameters is considered: $0 \leq Va \leq 20$ [37], $0 \leq Ta \leq 50$ [22], $0 \leq Ha \leq 0.9$ [40], and $0 \leq Dm \leq 20$ [23].

First, we shall discuss the theory of bifurcation points in Figures 5–7, the results obtained numerically by linear and weakly nonlinear stability analysis. Takens–Bogdanov and codimension two bifurcation points are identified in these figures. Takens–Bogdanov bifurcation point is the point at which the oscillatory neutral curve intersects the stationary neutral curve and approaches zero as the intersection point is approached. At the Takens–Bogdanov bifurcation point, we have

$$R_s(q_s) = R_o(q_o) \text{ and } q_s = q_o. \tag{33}$$

The codimension two bifurcation point is the intersection between a Hopf and Pitchfork bifurcation with distinct wave numbers. At the codimension two bifurcation point, we have

$$R_s(q_s) = R_o(q_o) \text{ and } q_s \neq q_o. \tag{34}$$

The effect of the Vadasz number *Va* on the neutral curves is presented in Figure 8. We find that the Ra_c^{sc} is independent of the Vadasz number *Va*, whereas the Ra_c^{oc} decreases with a decrease in the value of the Vadasz number *Va*. This reports the porosity effects on driven convection in a Newtonian-fluid-saturated porous layer. Furthermore, from this figure, one can notice that for $Va = 1$, there exists a threshold $Ta^* \in (1.9, 2)$ such that for $Ta < Ta^*$, stationary convection sets in, while for $Ta^* \in (1.9, 2)$, there is a switch from stationary to oscillatory convection. Similar behavior can be observed for the other values of *Va*.
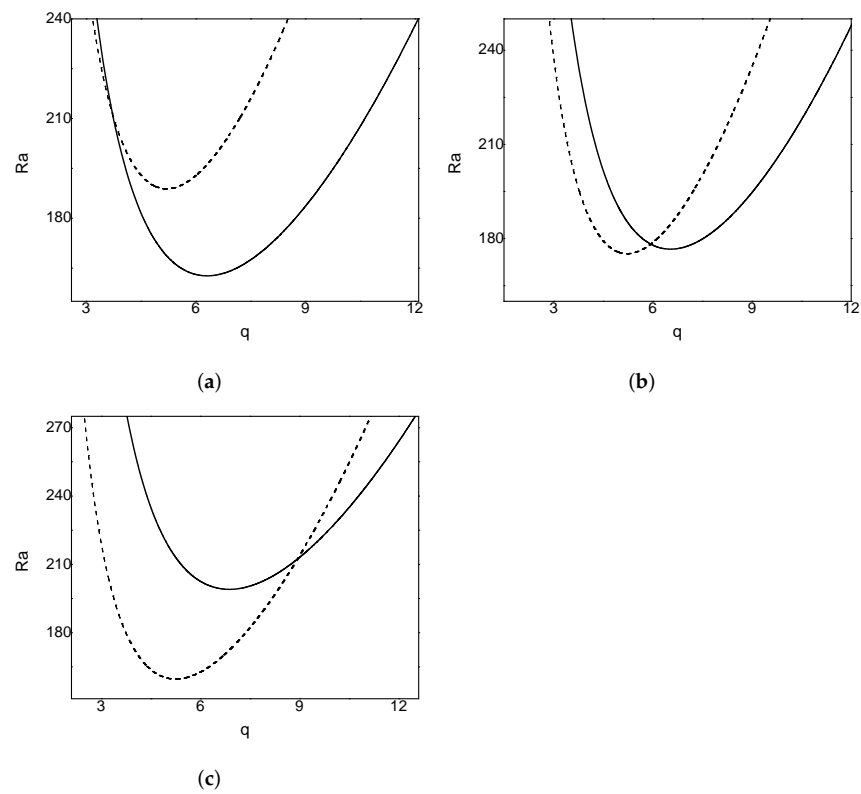
Figure 5. Neutral curves (solid lines represent the stationary convection and dotted lines represent the oscillatory convection) for $Dm = 20$, $Ta = 3.1$, $Va = 20$: (**a**) $Ha = 0.5$, (**b**) $Ha = 0.6$, (**c**) $Ha = 0.7$.
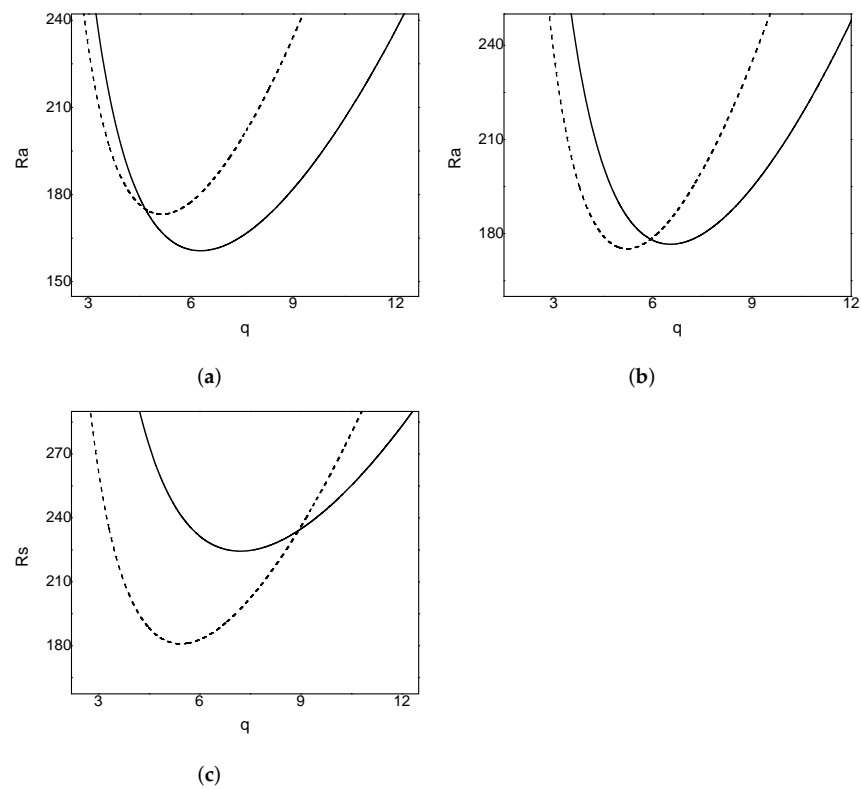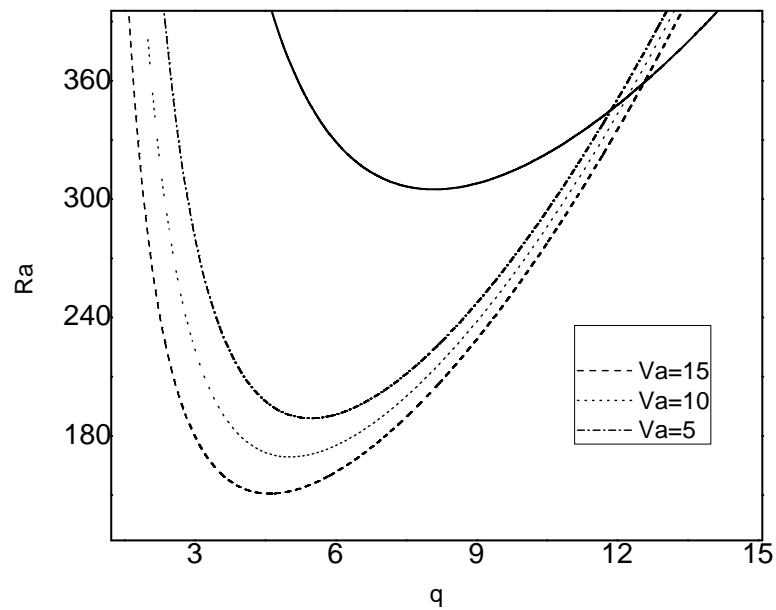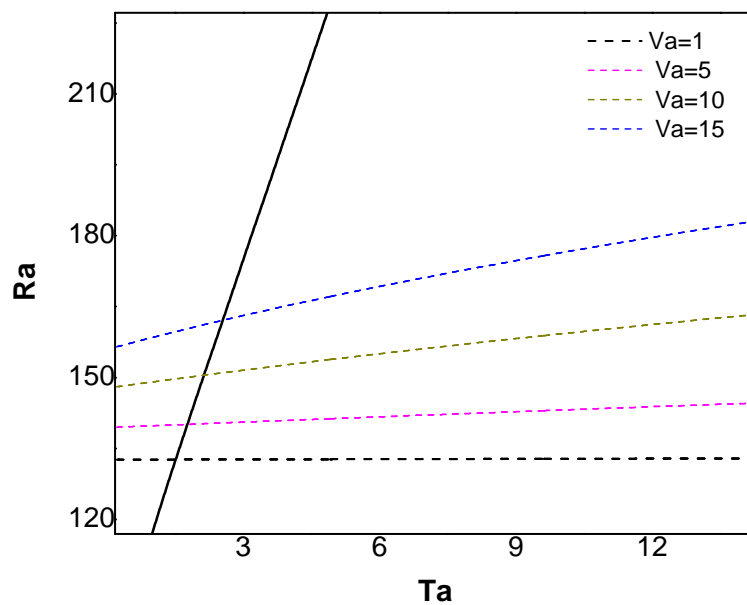

Figure 6. Neutral curves (solid lines represent the stationary convection and dotted lines represent the oscillatory convection) for $Dm = 20$, $Ha = 0.6$, $Va = 20$: (**a**) $Ta = 2.5$, (**b**) $Ta = 3.1$, (**c**) $Ta = 5$.

Figure 7. Neutral curves (solid lines represent the stationary convection and dotted lines represent the oscillatory convection) for $Dm = 20$, $Ha = 0.5$, $Ta = 10$.

Figure 8. Plots of the critical Ra as the function of Ta for $Va = 1, 5, 10, 15$.

Figure 9 illustrates the effect of the magnetic field on the onset of convection. From this figure, one can observe that the Hartmann number has a stabilizing effect on stationary convection. On the contrary, the Hartmann number has a stabilizing effect on oscillatory convection. We find that the minimum value of the stationary Rayleigh number for stationary mode increases with increasing Hartmann number Ha. On the other hand, the minimum value of the oscillatory Rayleigh number decreases with an increase in the value of the Hartmann number Ha. Thus, Ha has a contrasting effect on the stability of the system in the case of stationary and oscillatory modes. From this figure, we notice that for $Ha = 0.2$, there exists a threshold $Ta^* \in (1.9, 2)$ such that for $Ta < Ta^*$, oscillatory

convection sets in, while for $Ta^* \in (1.9, 2)$, there is a switch from oscillatory to stationary convection. Similar behavior can be observed for the other values of Va.
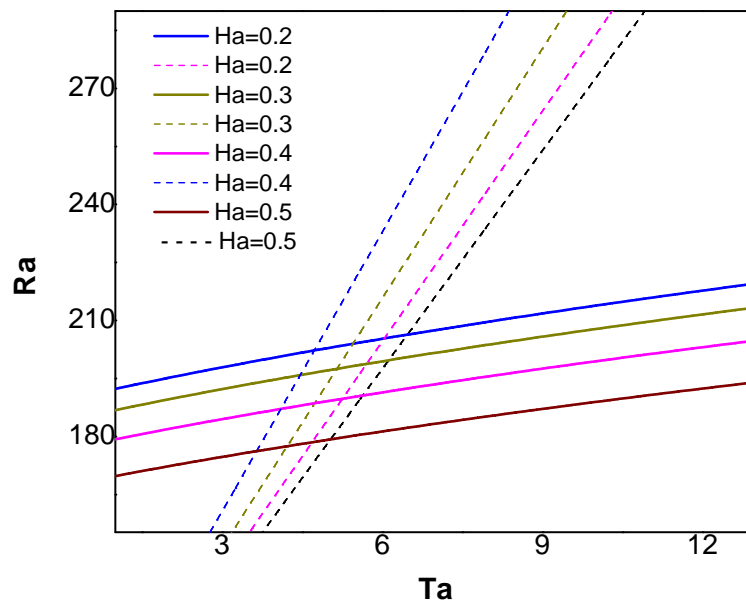

Figure 9. Plots of critical Ra as the function of Ta for $Dm = 5$, $Va = 5$, $Ha = 0.2$, 0.3, 0.4, 0.5.
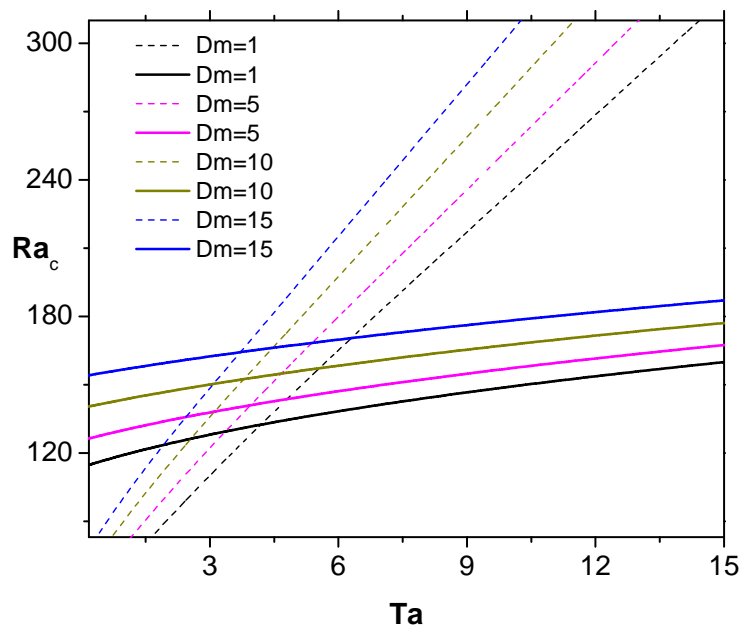

Figure 10. Plots of critical Ra as the function of Ta for $Va = 15$, $Ha = 0.5$, $Dm = 1$, 5, 10, 15.

Similarly, Figure 10 depicts the effect of Dm on the system. From this figure, we see that the effect of increasing Dm is to increase the Ra_c^{sc} and Ra_c^{oc}, implying that Dm has a stabilizing effect on the onset of dissolution-driven convection in a porous medium. This can be explained as follows. An increase in the value of Dm promotes the dissolution reaction to absorb some of the heat energy, causing the surrounding environment to feel cold. Hence, a larger solute gradient is required for the onset of convection so that the system is stabilized. We find that for fixed values of other physical parameters, there exists a critical Taylor number Ta_c such that when $Ta < Ta_c$, convection begins as an oscillatory type, and when $Ta > Ta_c$, the convection switches to stationary. Further, when $Ta = Ta_c$, the stationary and oscillatory modes occur simultaneously.

Furthermore, Figures 8–10 demonstrate the Coriolis effect on the onset of convection. All of these figures show that the Ra_c^{sc} and Ra_c^{oc} increase as the Taylor number increases. Hence, the Taylor number has a stabilizing effect on the system. This can be explained as follows: in the fluid, the rotation creates vorticity. As a result, the fluid has a faster velocity in horizontal planes. Hence, the perpendicular velocity of the fluid decreases. Therefore, the convection does not start right away.

The comparison of numerical and predicted ANN data of the critical Ra with different values of Va, Ha, Ta, and Dm is shown in Figures 11 and 12. From all these figures, it is obvious to see that the trained predictive ANN model holds well with the numerical results.
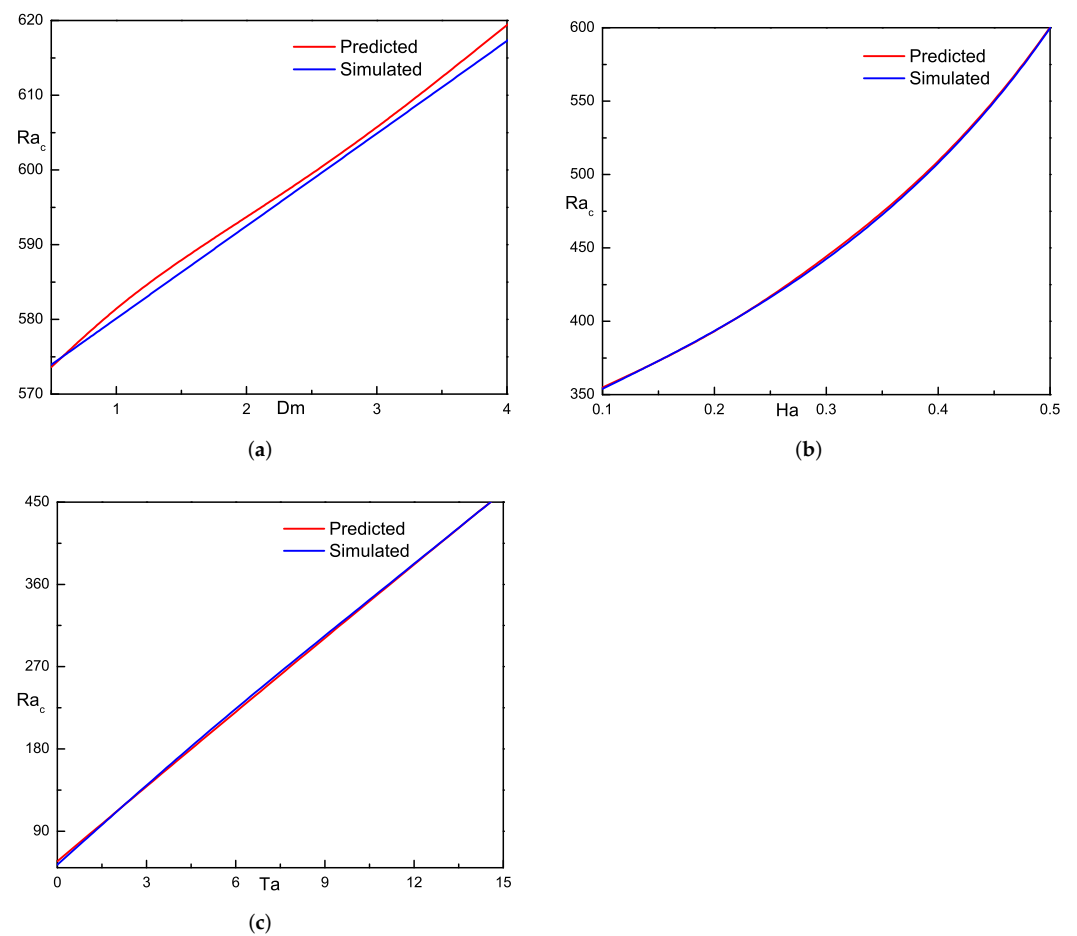
Figure 11. Comparison of the simulated and ANN-predicted critical Rayleigh number values for (**a**) *Dm*, (**b**) *Ha*, and (**c**) *Ta*.
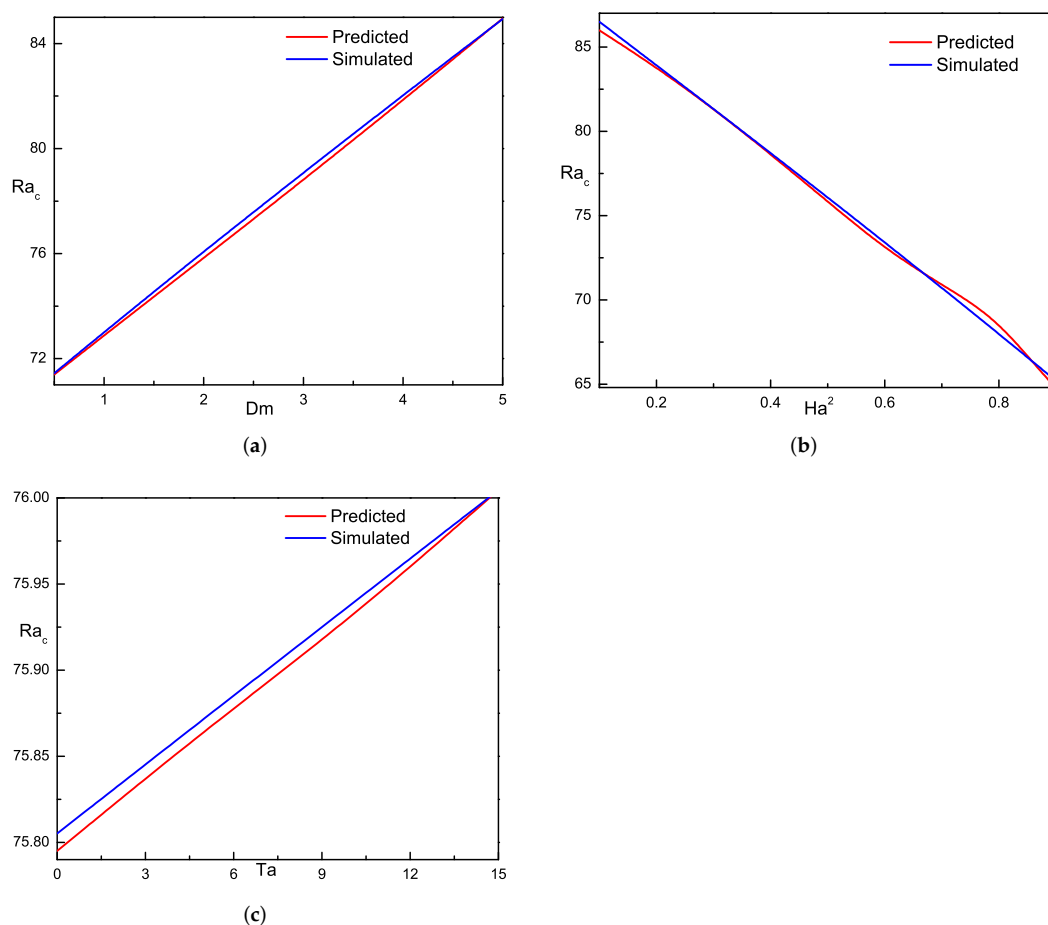
Figure 12. Comparison of the simulated and ANN-predicted critical Rayleigh number values for
(**a**) *Dm*, (**b**) *Ha*, and (**c**) *Ta*.

5. Conclusions

In the present analysis, the onset of dissolution-driven convection in a porous layer
with the effect of the magnetic field and rotation is studied. The behavior of various physical
parameters is investigated. The results can be summarized as follows: Takens–Bogdanov
and codimension two bifurcation points are identified. The Vadasz number does not show
any effect on stationary convection, whereas it has a destabilizing effect on oscillatory
convection. The Hartmann number has destabilizing and stabilizing effects on stationary
and oscillatory convection, respectively. The Damkohler number has a stabilizing effect on
the system. Furthermore, an artificial neural network (ANN) is used to model and predict
the critical Rayleigh numbers. The simulated and predicted values of the proposed ANN
model were found to be highly close, indicating that the expected critical Rayleigh number
and the observed critical Rayleigh number are quite similar.

In future work, we plan to study linear instability and nonlinear stability. Another
interesting problem is to investigate the stationary or oscillatory convection at the onset of
instability using Brinkmann's law.

Author Contributions: Conceptualization, G.S.K.R. and N.V.K.; methodology, G.S.K.R., N.V.K., R.R.,
K.K.P. and C.C.; software, G.S.K.R., N.V.K., R.R., K.K.P. and C.C.; validation, G.S.K.R., N.V.K., R.R.,
K.K.P. and C.C.; formal analysis, G.S.K.R., N.V.K., R.R., K.K.P. and C.C.; investigation, G.S.K.R., N.V.K.,
R.R., K.K.P. and C.C.; resources, G.S.K.R., N.V.K., R.R., K.K.P. and C.C.; data curation, G.S.K.R., N.V.K.,
R.R., K.K.P. and C.C.; writing—original draft preparation, G.S.K.R., N.V.K., R.R., K.K.P. and C.C.;
writing—review and editing, G.S.K.R., N.V.K., R.R., K.K.P. and C.C.; visualization, G.S.K.R., N.V.K.,
R.R., K.K.P. and C.C. All authors have read and agreed to the published version of the manuscript.

References

1. Ghoshal, P.; Kim, M.C.; Cardoso, S.S. Reactive–convective dissolution in a porous medium: the storage of carbon dioxide in saline aquifers. *Phys. Chem. Chem. Phys.* **2017**, *19*, 644–655. [CrossRef] [PubMed]
2. Ilya, A.; Ashraf, M.; Ali, A.; Shah, Z.; Kumam, P.; Thounthong, P. Heat source and sink effects on periodic mixed convection flow along the electrically conducting cone inserted in porous medium. *PLoS ONE* **2021**, *16*, e0260845. [CrossRef] [PubMed]
3. Alshehri, A.; Shah, Z. Computational analysis of viscous dissipation and Darcy-Forchheimer porous medium on radioactive hybrid nanofluid. *Case Stud. Therm. Eng.* **2022**, *30*, 101728. [CrossRef]
4. Vo, D.D.; Shah, Z.; Sheikholeslami, M.; Shafee, A.; Nguyen, T.K. Numerical investigation of MHD nanomaterial convective migration and heat transfer within a sinusoidal porous cavity. *Phys. Scr.* **2019**, *94*, 115225. [CrossRef]
5. Jamshed, W.; Şirin, C.; Selimefendigil, F.; Shamshuddin, M.D.; Altowairqi, Y.; Eid, M.R. Thermal Characterization of Coolant Maxwell Type Nanofluid Flowing in Parabolic Trough Solar Collector (PTSC) Used Inside Solar Powered Ship Application. *Coatings* **2021**, *11*, 1552. [CrossRef]
6. Mahabaleshwar, U.S.; Rekha, M.B.; Kumar, P.N.V.; Selimefendigil, F.; Sakanaka, P.H.; Lorenzini, G.; Nayakar, S.N.R. Mass transfer characteristics of MHD casson fluid flow past stretching/shrinking sheet. *J. Eng. Thermophys.* **2020**, *29*, 285–302. [CrossRef]
7. Steinberg, V.; Brand, H. Convective instabilities of binary mixtures with fast chemical reaction in a porous medium. *J. Chem. Phys.* **1983**, *78*, 2655–2660. [CrossRef]
8. Steinberg, V.; Brand, H.R. Amplitude equations for the onset of convection in a reactive mixture in a porous medium. *J. Chem. Phys.* **1984**, *80*, 431–435. [CrossRef]
9. Gatica, J.E.; Viljoen, H.J.; Hlavacek, V. Interaction between chemical reaction and natural convection in porous media. *Chem. Eng. Sci.* **1989**, *44*, 1853–1870. [CrossRef]
10. Pritchard, D.; Richardson, C.N. The effect of temperature-dependent solubility on the onset of thermosolutal convection in a horizontal porous layer. *J. Fluid Mech.* **2007**, *571*, 59–95. [CrossRef]
11. Rees, D.A.S.; Selim, A.; Ennis-King, J. *The Instability of Unsteady Boundary Layers in Porous Media*; Springer: Berlin/Heidelberg, Germany, 2008.
12. Slim, A.C.; Ramakrishnan, T. Onset and cessation of time-dependent, dissolution-driven convection in porous media. *Phys. Fluids* **2010**, *22*, 124103. [CrossRef]
13. Bestehorn, M.; Firoozabadi, A. Effect of fluctuations on the onset of density-driven convection in porous media. *Phys. Fluids* **2012**, *24*, 114102. [CrossRef]
14. Kim, M.C.; Choi, C.K. Effect of first-order chemical reaction on gravitational instability in a porous medium. *Phys. Rev. E* **2014**, *90*, 053016. [CrossRef] [PubMed]
15. Hill, A.A.; Morad, M.R. Convective stability of carbon sequestration in anisotropic porous media. *Proc. R. Soc. Math. Phys. Eng. Sci.* **2014**, *470*, 20140373. [CrossRef]
16. Al-Sulaimi, B. The energy stability of Darcy thermosolutal convection with reaction. *Int. J. Heat Mass Transf.* **2015**, *86*, 369–376. [CrossRef]
17. Emami-Meybodi, H. Stability analysis of dissolution-driven convection in porous media. *Phys. Fluids* **2017**, *29*, 014102. [CrossRef]
18. Salibindla, A.K.; Subedi, R.; Shen, V.C.; Masuk, A.U.; Ni, R. Dissolution-driven convection in a heterogeneous porous medium. *J. Fluid Mech.* **2018**, *857*, 61–79. [CrossRef]
19. Gautam, K.; Narayana, P.A.L. On the stability of carbon sequestration in an anisotropic horizontal porous layer with a first-order chemical reaction. *Proc. R. Soc. A* **2019**, *475*, 20180365. [CrossRef]
20. Babu, A.B.; Koteswararao, N.V.; Reddy, G.S. Instability conditions in a porous medium due to horizontal magnetic field. In *Numerical Heat Transfer and Fluid Flow*; Springer: Singapore, 2019; pp. 621–628.
21. Babu, A.B.; Rao, N.; Tagare, S.G. Weakly nonlinear thermohaline convection in a sparsely packed porous medium due to horizontal magnetic field. *Eur. Phys. J. Plus* **2021**, *136*, 795. [CrossRef]
22. Babu, A.B.; Anilkumar, D.; Rao, N.V.K. Weakly nonlinear thermohaline rotating convection in a sparsely packed porous medium. *Int. J. Heat Mass Transf.* **2022**, *188*, 122602. [CrossRef]
23. Reddy, G.S.K.; Ragoju, R. Thermal instability of a Maxwell fluid saturated porous layer with chemical reaction. *Spec. Top. Rev. Porous Media Int. J.* **2022**, *13*, 33–47. [CrossRef]
24. Yin, Y.; Qu, Z.; Zhu, C.; Zhang, J. Visualizing gas diffusion behaviors in three-dimensional nanoporous media. *Energy Fuels* **2021**, *35*, 2075–2086. [CrossRef]
25. Yin, Y.; Qu, Z.; Prodanović, M.; Landry, C.J. Identifying the dominant transport mechanism in single nanoscale pores and 3D nanoporous media. *Fundam. Res.* **2022**. [CrossRef]
26. Utech, H.P.; Flemmings, M.C. Elimination of solute banding in indium antimonide crystals by growth in a magnetic field. *J. Appl. Phys.* **1966**, *37*, 2021–2024. [CrossRef]
27. Vives, C.; Perry, C. Effects of magnetically damped convection during the controlled solidification of metals and alloys. *Int. J. Heat Mass Transf.* **1987**, *30*, 479–496. [CrossRef]

28. Garandet, J.P.; Alboussiere, T.; Moreau, R. Buoyancy driven convection in a rectangular enclosure with a transverse magnetic field. *Int. J. Heat Mass Transf.* **1992**, *35*, 741–748. [CrossRef]

29. Alboussiere, T.; Garandet, J.P. Buoyancy-driven convection with a uniform magnetic field. Part 1. Asymptotic analysis. *J. Fluid Mech.* **1993**, *253*, 545–563. [CrossRef]

30. Rudraiah, N.; Venkatachalappa, M.; Subbaraya, C.K. Combined surface tension and buoyancy-driven convection in a rectangular open cavity in the presence of a magnetic field. *Int. J. Non-Linear Mech.* **1995**, 30, 759–770. [CrossRef]

31. Davoust, L.; Cowley, M.D.; Moreau, R.; Bolcato, R. Buoyancy-driven convection with a uniform magnetic field. Part 2. Experimental investigation. *J. Fluid Mech.* **1999**, *400*, 59–90. [CrossRef]

32. Priede, J.; Gerbeth, G. Hydrothermal wave instability of thermocapillary-driven convection in a transverse magnetic field. *J. Fluid Mech.* **2000**, *404*, 211–250. [CrossRef]

33. Pirmohammadi, M.; Ghassemi, M.; Sheikhzadeh, G.A. The effect of a magnetic field on buoyancy-driven convection in differentially heated square cavity. In Proceedings of the 2008 14th Symposium on Electromagnetic Launch Technology, Victoria, BC, Canada, 10–13 June 2008; pp. 1–6.

34. Sankar, M.; Venkatachalappa, M.; Do, Y. Effect of magnetic field on the buoyancy and thermocapillary driven convection of an electrically conducting fluid in an annular enclosure. *Int. J. Heat Fluid Flow* **2011**, *32*, 402–412. [CrossRef]

35. Erglis, K.; Tatulcenkov, A.; Kitenbergs, G.; Petrichenko, O.; Ergin, F.G.; Watz, B.B.; Cbers, A. Magnetic field driven micro-convection in the Hele–Shaw cell. *J. Fluid Mech.* **2013**, *714*, 612–633. [CrossRef]

36. Babu, A.B.; Reddy, G.S.K.; Tagare, S.G. Nonlinear magneto convection due to horizontal magnetic field and vertical axis of rotation due to thermal and compositional buoyancy. *Results Phys.* **2019**, *12*, 2078–2090. [CrossRef]

37. Govender, S.; Vadasz, P. The effect of mechanical and thermal anisotropy on the stability of gravity driven convection in rotating porous media in the presence of thermal non-equilibrium. *Transp. Porous Media* **2007**, *69*, 55–66. [CrossRef]

38. Babu, A.B.; Reddy, G.S.K.; Tagare, S.G. Nonlinear magnetoconvection in a rotating fluid due to thermal and compositional buoyancy with anisotropic diffusivities. *Heat Transf. Asian Res.* **2020**, *49*, 335–355. [CrossRef]

39. Wang, S.; Wenchang, T. The onset of Darcy–Brinkman thermosolutal convection in a horizontal porous media. *Phys. Lett. A* **2009**, *373*, 776–780. [CrossRef]

40. Deepika, N.; Murthy, P.V.S.N.; Narayana, P.A.L. The effect of magnetic field on the stability of double-diffusive convection in a porous layer with horizontal mass throughflow. *Transp. Porous Media* **2020**, *134*, 435–452. [CrossRef]

41. Horton, C.W.; Rogers, F.T. Convection currents in a porous medium. *J. Appl. Phys.* **1945**, *16*, 367–370. [CrossRef]

42. Lapwood, E.R. Convection of a fluid in a porous medium. *Math. Proc. Camb. Philos. Soc.* **1948**, *44*, 508–521. [CrossRef]

43. Dey, P.; Abhijit, S.; Das, A.K. Development of GEP and ANN model to predict the unsteady forced convection over a cylinder. *Neural Comput. Appl.* **2016**, *27*, 2537–2549. [CrossRef]

44. Rana, P.; Gupta, V.; Kumar, L. LTNE magneto-thermal stability analysis on rough surfaces utilizing hybrid nanoparticles and heat source with artificial neural network prediction. *Appl. Nanosci.* **2021**. [CrossRef]

45. Seo, Y.M.; Pandey, S.; Lee, H.U.; Choi, C.; Park, Y.G.; Ha, M.Y. Prediction of heat transfer distribution induced by the variation in vertical location of circular cylinder on Rayleigh-Bénard convection using artificial neural network. *Int. J. Mech. Sci.* **2021**, *209*, 106701. [CrossRef]

46. Yu, H.; Wilamowski, B.M. Levenberg–Marquardt training. In *Intelligent Systems*; CRC Press: Boca Raton, FL, USA, 2018; Chapter 12, pp. 1–16.

47. Seo, Y.M.; Luo, K.; Ha, M.Y.; Park, Y.G. Direct numerical simulation and artificial neural network modeling of heat transfer characteristics on natural convection with a sinusoidal cylinder in a long rectangular enclosure. *Int. J. Heat Mass Transf.* **2020**, *152*, 119564. [CrossRef]

48. Khosravi, R.; Rabiei, S.; Bahiraei, M.; Teymourtash, A.R. Predicting entropy generation of a hybrid nanofluid containing graphene–platinum nanoparticles through a microchannel liquid block using neural networks. *Int. Commun. Heat Mass Transf.* **2019**, *109*, 104351. [CrossRef]

49. Amani, M.; Amani, P.; Bahiraei, M.; Wongwises, S. Prediction of hydrothermal behavior of a non-Newtonian nanofluid in a square channel by modeling of thermophysical properties using neural network. *J. Therm. Anal. Calorim.* **2019**, *135*, 901–910. [CrossRef]

50. Bahiraei, M.; Heshmatian, S.; Keshavarzi, M. Multi-criterion optimization of thermohydraulic performance of a mini pin fin heat sink operated with ecofriendly graphene nanoplatelets nanofluid considering geometrical characteristics. *J. Mol. Liq.* **2019**, *276*, 653–666. [CrossRef]

51. Bahiraei, M.; Mazaheri, N.; Hosseini, S. Neural network modeling of thermo-hydraulic attributes and entropy generation of an ecofriendly nanofluid flow inside tubes equipped with novel rotary coaxial double-twisted tape. *Powder Technol.* **2020**, *369*, 162–175. [CrossRef]